nature communications

Article

https://doi.org/10.1038/s41467-024-50722-1

Elucidating the Architectural dynamics of MuB filaments in bacteriophage Mu DNA transposition

Received: 19 February 2024

Accepted: 18 July 2024

Published online: 31 July 2024

Check for updates

Xiaolong Zhao[1], Yongxiang Gao[1], Qingguo Gong[1], Kaiming Zhang[1] ✉ & Shanshan Li[1] ✉

MuB is a non-specific DNA-binding protein and AAA+ ATPase that significantly influences the DNA transposition process of bacteriophage Mu, especially in target DNA selection for transposition. While studies have established the ATP-dependent formation of MuB filament as pivotal to this process, the high-resolution structure of a full-length MuB protomer and the underlying molecular mechanisms governing its oligomerization remain elusive. Here, we use cryo-EM to obtain a 3.4-Å resolution structure of the ATP(+)-DNA(+)-MuB helical filament, which encapsulates the DNA substrate within its axial channel. The structure categorizes MuB within the initiator clade of the AAA+ protein family and precisely locates the ATP and DNA binding sites. Further investigation into the oligomeric states of MuB show the existence of various forms of the filament. These findings lead to a mechanistic model where MuB forms opposite helical filaments along the DNA, exposing potential target sites on the bare DNA and then recruiting MuA, which stimulates MuB's ATPase activity and disrupts the previously formed helical structure. When this happens, MuB generates larger ring structures and dissociates from the DNA.

Bacteriophage Mu (Mu), a member of the Myxoviridae family, demonstrates a broad spectrum of infectivity across various bacterial species[1]. The genesis of Mu research dates back to the 1960s, with a pivotal discovery in 1963 by Larry Taylor, who accidentally isolated a mild bacteriophage capable of inducing mutations in *E. coli*, subsequently named mutant Mu[2]. Further studies have elucidated that Mu is one of the most intricate and efficient DNA transposons, which can move and insert itself into the bacterial genome. DNA transposition is not only fundamental to the evolution and diversity of genomes but also has significant implications for the development of antibiotic resistance and the spread of virulence factors among bacteria. The investigation into Mu has laid the foundation for understanding the transposition mechanism, retroviral integration, and early steps in V(D)J recombination[3–7].

To conduct effective Mu transposition, interactions between two phage proteins, MuA (DDE recombinase A) and MuB (ATP-dependent target DNA activator B), are necessary, and these proteins must form complex structures with DNA[8]. MuA initially identifies and binds to the ends of the Mu genome, taking them close together to create a stable structure called the transpososome. MuA then cleaves the Mu ends and integrates them into a new target DNA site[9–11]. On the other hand, MuB acts as an essential activator, facilitating MuA's assembly at the Mu ends[8], enhancing MuA's catalytic activity[12], and assisting in the delivery of target DNA to the transpososome[13].

Belonging to the AAA+ (ATPases Associated with Diverse Cellular Activities) ATPase family, MuB is crucial in the DNA transposition process by forming helical filaments, especially in selecting target DNA[14]. This activity is tied to its oligomeric nature. When acting as a

[1]Department of Urology, The First Affiliated Hospital of USTC, MOE Key Laboratory for Cellular Dynamics, Center for Advanced Interdisciplinary Science and Biomedicine of IHM, Division of Life Sciences and Medicine, University of Science and Technology of China, Hefei, China. ✉e-mail: kmzhang@ustc.edu.cn; lishanshan@ustc.edu.cn

monomer, MuB activates and assembles MuA at the Mu ends[8,12]. Its polymeric form, controlled by the presence of ATP, is vital for target selection. Phage Mu benefits from MuB's defense mechanism against self-integration, enabling the selection of appropriate target DNA[15–17]. After integrating into the bacterial genome, phage Mu employs a replicative-transposition mechanism to amplify its genome, which can result in a substantial accumulation of Mu DNA[18–24].

To date, structural research of MuB has lagged far behind biochemical analysis, limiting the understanding of its function. Initial nuclear magnetic resonance (NMR) investigations provided partial insights, revealing only segments of MuB's N-terminal[25] and C-terminal[26] sequences. This led to an incomplete understanding of its overall structure. The dynamics of MuB-DNA interactions were first observed using total internal reflection fluorescence (TIRF) microscopy, demonstrating that ATP-bound GFP-MuB forms short, separate filaments along the DNA, which elongate with increasing protein concentration[27,28]. Later, Mizuno et al.'s work[14], utilizing cryo-electron microscopy (cryo-EM), revealed the right-handed helical architecture of MuB filaments and their non-deformative interaction with DNA, setting the stage for further investigations into the complex mechanisms of MuB-mediated DNA transposition. However, despite these significant advances, certain limitations were noted, including the resolution of the cryo-EM structure (~17 Å), which precluded the visualization of atomic-level details, and a comprehensive understanding of the dynamic processes underlying MuB filament assembly and disassembly during transposition.

In our study, we have achieved a 3.4-Å resolution of the MuB filament using cryo-EM, offering atomic-level structural details of MuB within the helical filament and revealing various oligomeric states. Acknowledging the high heterogeneity in MuB assembly previously described by Mizuno et al., it is important to consider the possibility that our analysis might not capture all potential conformations. However, the high-resolution structure has allowed us to observe the intricate interactions between MuB subunits and how these interactions facilitate the formation of the filamentous structure. Furthermore, our study sheds light on the mechanism by which MuB interacts with DNA during the transposition cycle, particularly in terms of its binding of DNA for target site selection. These findings suggest a molecular model to explain MuB targeting DNA for transposition. This comprehensive structural insight into the MuB filament not only unveils the dynamic nature of this protein but also advances our knowledge of the Mu transposition system.

Results

Visualization of MuB filaments by negative-staining electron microscopy

Given MuB's propensity to aggregate in the presence of ATP, we opted to explore these aggregates using negative-staining electron microscopy. To assemble MuB filament suitable for structural analysis, a range of experimental conditions such as temperature, expression tag, salt concentration, and mixing method were systematically investigated. After careful evaluation, it was determined that a salt concentration of 300 mM proved to be the most conducive for optimal filament assembly (Supplementary Fig. 1), which was also reported by Mizuno et al. [14].

The experiments yielded insightful results regarding the role of nucleotide and DNA in the formation of MuB filaments. It was observed that neither ATP nor DNA alone could induce the formation of MuB filaments. However, when DNA was present, the addition of ATP initiated the polymerization of MuB into elongated filaments. Conversely, the introduction of ADP resulted in the formation of shorter and irregular filaments (Supplementary Fig. 2). These findings indicate that ATP and ADP lead to distinct filament formations, likely representing different phases of MuB's functionality during the Mu transposition process.

Cryo-EM helical reconstruction of ATP-induced DNA(+) MuB filaments

To delineate the structural interactions and assembly process of MuB filaments, we employed cryo-EM to examine vitrified ATP(+)-DNA(+)-MuB filament samples. This analysis was pivotal in providing substantial insights into the filament architecture. A total of 5439 micrographs were selected after motion correction and CTF estimation (Supplementary Fig. 3). Helical segments were then automatically picked and extracted in a box of 336 × 336 pixels. Subsequent two-dimensional (2D) classifications revealed well-defined helical filaments, prompting us to employ helical refinement using cryoSPARC[29]. The helical parameters were characterized by a helical rise of 6.913 Å and a helical twist of 56.156°, corresponding to 6.41 asymmetric units per helical turn and a 44.32 Å helical pitch (Fig. 1a). The final helical refinement led to a 3.4-Å resolution reconstruction of the ATP(+)-DNA(+)-MuB filament, which exhibited a right-handed helical architecture (Fig. 1a, Supplementary Fig. 3, and Supplementary Movie 1).

The DNA substrate within the MuB filament is embedded in the axial channel, adopting a configuration (12.82 bp and 44.32 Å per turn) that deviates from the typical B-form DNA (Fig. 1a). We elucidate that while this configuration differs from the typical B-form, the alteration to the DNA structure is subtle, and MuB does not induce a significant distortion in the DNA duplex. This nuanced configuration suggests a minor deviation rather than a pronounced deformation, warranting further exploration to fully understand its implications. We propose that this subtle deviation introduces a level of potential energy into the DNA, which may play a crucial role in stabilizing MuB's attachment to the target site and aiding MuA during the forward transposition process. This concept is in line with mechanisms observed in integrases, where DNA distortions serve as a facilitator for their functions[30].

The atomic structure of MuB possesses a canonical AAA+ fold

At an overall resolution of 3.4 Å, we have successfully built a near-complete molecular model of the MuB protomer, encompassing residues from L67 to N312, and then the atomically detailed structure of the MuB filament (Figs. 1b, c and 2a and Supplementary Fig. 4). As mentioned, MuB is classified as an AAA+ ATPase[14], a group of proteins that utilize the energy from ATP hydrolysis to perform various cellular functions. Structurally, MuB consists of two main components: the AAA+ module and the N-terminal domain (NTD)[14]. The AAA + module, as elucidated in our study, is further subdivided into α/β and α subdomains. The α/β subdomain features a central β-sheet organized in a β5-β1-β4-β3-β2 sequence. This β-sheet is flanked by α-helices, resulting in a layered α-β-α sandwich configuration. Concurrently, the α subdomain contains a four-helix bundle (Fig. 2a–c). Both subdomains are integral to the formation of the nucleotide-binding site and facilitate inter-subunit interactions within oligomeric protein assemblies[31]. In terms of structural classification, MuB aligns with the initiator clade, a distinction marked by an additional α-helix known as the initiator-specific motif (ISM), positioned between α2 and β2 in the α-β-α core[31] (Fig. 2b, c).

Previous research has indicated that the NTD of MuB adopts a conformation of four compact α-helices, characterized by a helix-turn-helix (HTH) motif[25]. While we observed some features of the NTD in the 2D classes of the ATP(+)-DNA(+)-MuB filament (Fig. 2d), the NTD was not visible in our final reconstruction. This invisibility likely results from its flexible linkage to the AAA+ module, mirroring observations from the previous study[14]. These findings suggest a dynamic interaction between these structural components.

Identification of residues critical for MuB helical filament formation

The atomically detailed structure of the MuB filament enables us to analyze the structural basis of how MuB polymerizes into long filaments on DNA. In an attempt to elucidate the assembly mechanism of MuB, we have demarcated a fundamental unit comprising three MuB subunits

https://doi.org/10.1038/s41467-024-50722-1

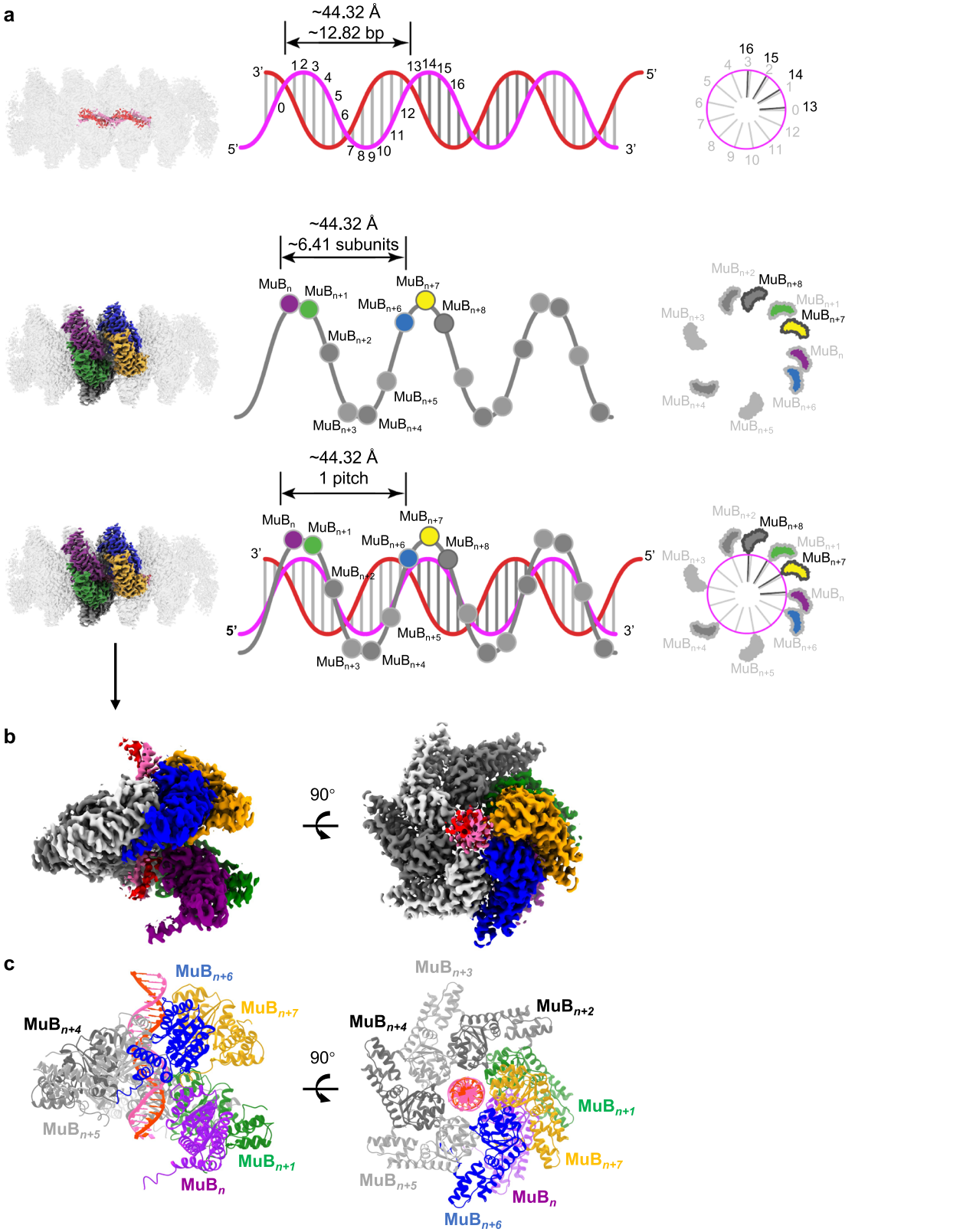

Fig. 1 | Overall structure of the ATP(+)-DNA(+)-MuB helical filament. a The ATP(+)-DNA(+)-MuB helix. Left: cryo-EM map; middle: cartoon display with the pitch parameters for DNA and MuB shown; right: top view. **b** Cryo-EM map of one helical turn containing eight MuB subunits and 24 bp dsDNA. **c** Atomic model of one helical turn containing eight MuB subunits and 24 bp dsDNA. DNA, MuB_n, MuB_{n+1}, MuB_{n+6}, and MuB_{n+7} are shown in different colors.

within the helical structure (Fig. 3a). We conducted a detailed examination of the molecular interplay among these subunits. For illustrative purposes, we designated one subunit as the central unit (MuB_n) and showcased its interactions with the two adjacent subunits (MuB_{n+1}, MuB_{n+6}). Using the PDBsum structure bioinformatics software[32] to analyze our structure model, we identified the key residues to engage in interactions between the subunits. As shown in Fig. 3b, the molecular interface mainly lies on the α/β subdomain of MuB_n, which interacts

https://doi.org/10.1038/s41467-024-50722-1

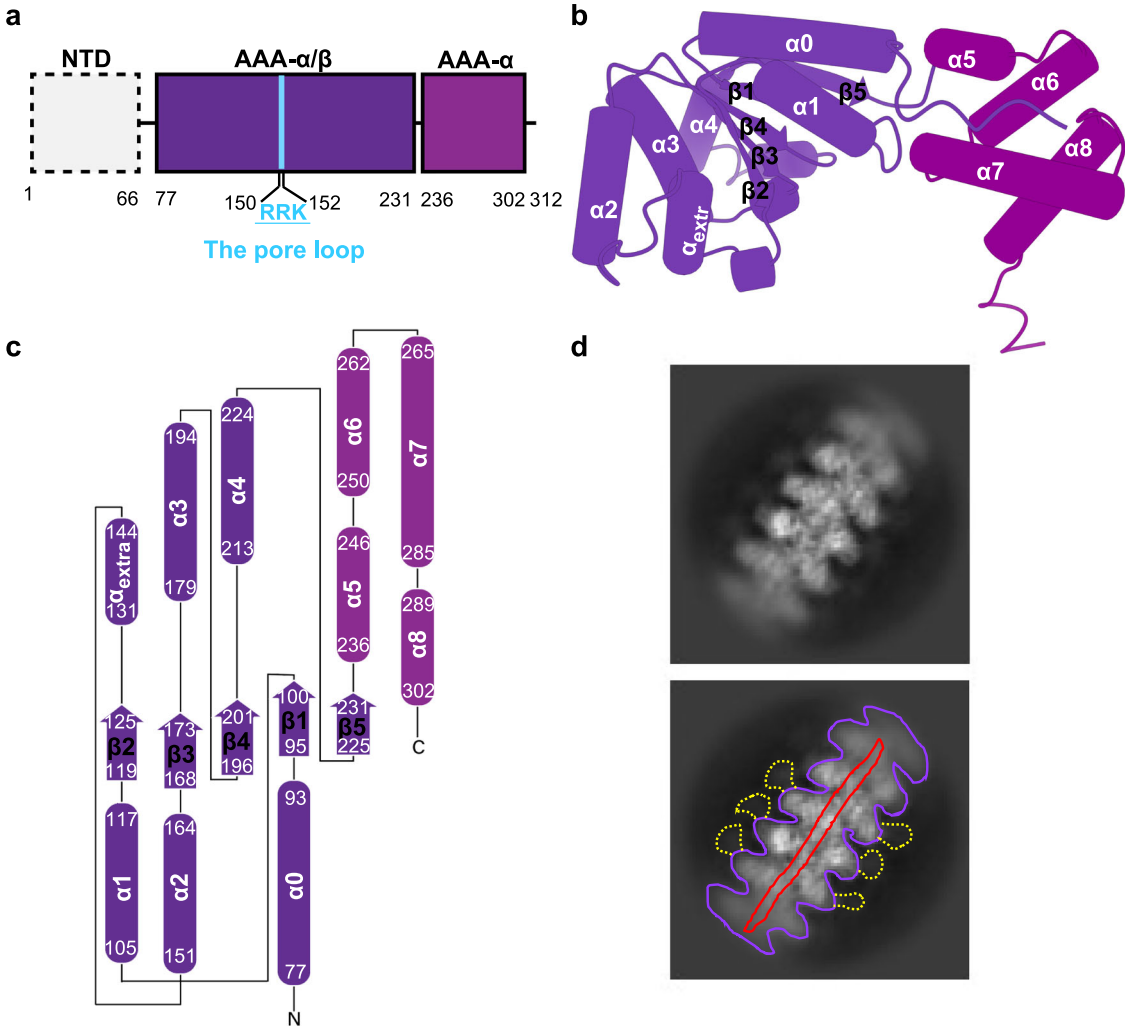

Fig. 2 | Cryo-EM structure of the MuB protomer in the helical filament. a Domain architecture of the MuB protomer. **b** Three-dimensional structure of the MuB protomer. **c** Secondary structure topology of the MuB protomer. MuB is characterized by an additional α-helix (α_{extra}) inserted between α2 and β2. **d** Representative 2D class of the ATP(+)-DNA(+)-MuB filament with the N-terminal domain (NTD) features. NTDs, DNA, and AAA+ modules are shown as yellow, red, and purple lines, respectively.

with the α/β subdomain, α subdomain, and C-terminus of MuB_{n+1}. The interface area between the α/β subdomains of MuB_n and MuB_{n+1} can reach ~1600 Å^2 and involves seven salt bridges and extensive hydrogen bonds (Fig. 3c–h). Molecular contacts between MuB_n and MuB_{n+6}, however, reveal a weak or promiscuous interaction (Fig. 3i). To validate these interactions, we conducted mutagenesis experiments targeting specific residues, including R157A, S128A/E134A/E138A, E174A/D176A/H177A, R220A/K227A/R228A/N232A, R268A, N101A/R111A, and deletion of residues 301–312 (Δ301 ~ 312). These mutations were designed to disrupt key interactions between MuB_n and MuB_{n+1}. Our results showed that the majority of these mutants were unable to form filaments (Supplementary Fig. 5a). Therefore, it is evident that interactions between contiguous subunits, such as MuB_n and MuB_{n+1}, are crucial for the filamentous assembly of MuB.

We next aimed to identify the precise binding sites of ATP and DNA, both of which are essential for inducing MuB filament formation (Supplementary Fig. 2). In our structural analysis, ATP is bound at the interface between the α/β and α subdomains, engaging with conserved residues characteristic of the majority of AAA+ proteins[31] (Fig. 4a–c and Supplementary Movie 2). The ATP molecule shows a strong cryo-EM density, with its base interacting with V74 in the α/β subdomain and its ribose interacting with N271 at the entrance of the ATPase pocket. The phosphate groups form extensive contacts with the Walker-A motif (e.g., T107) in the α/β subdomain and the β-phosphate contacts with the Sensor-II motif (e.g., R268) in the α subdomain (Fig. 4b). Moreover, the γ-phosphate of ATP interacts with the Arginine-finger R224 from the neighboring subunit (Fig. 4c). As reported, the Sensor-II and Arginine-finger residues both interacting with the γ-phosphate of ATP appear to position the scissile Pγ-Oβ bond of ATP in an optimal conformation for hydrolysis[33]. Therefore, the interactions of Sensor-II and Arginine-finger residues in our structure with β- and γ-phosphates, respectively, potentially result in the low ATPase activity of MuB[13]. Mutations in the Walker-A (T107A), Sensor-II (R268A), and Arginine-finger (R224A) residues significantly reduced the ATPase activity compared with the wild-type MuB (Fig. 4d), underscoring their importance in MuB's ATPase function.

In AAA+ proteins, pore loops within the central channel of the oligomeric ring formed by AAA+ domains play a critical role in substrate interaction and translocation[34–36]. In MuB, a loop containing residues R150/R151/K152 protruded from the helical ISM insertion associated with the initiator clade was identified to interact with the DNA substrate within the axial pore (Fig. 5a–d). These interactions occur with both strands of the DNA duplex, unlike the single-strand interactions observed in Tn7-like transposons[37]. Mutational analysis, including single (R151A, K152A), double (R150A/R151A, R151A/K152A), and triple (R150A/R151A/K152A) mutations, was performed. Notably,

https://doi.org/10.1038/s41467-024-50722-1

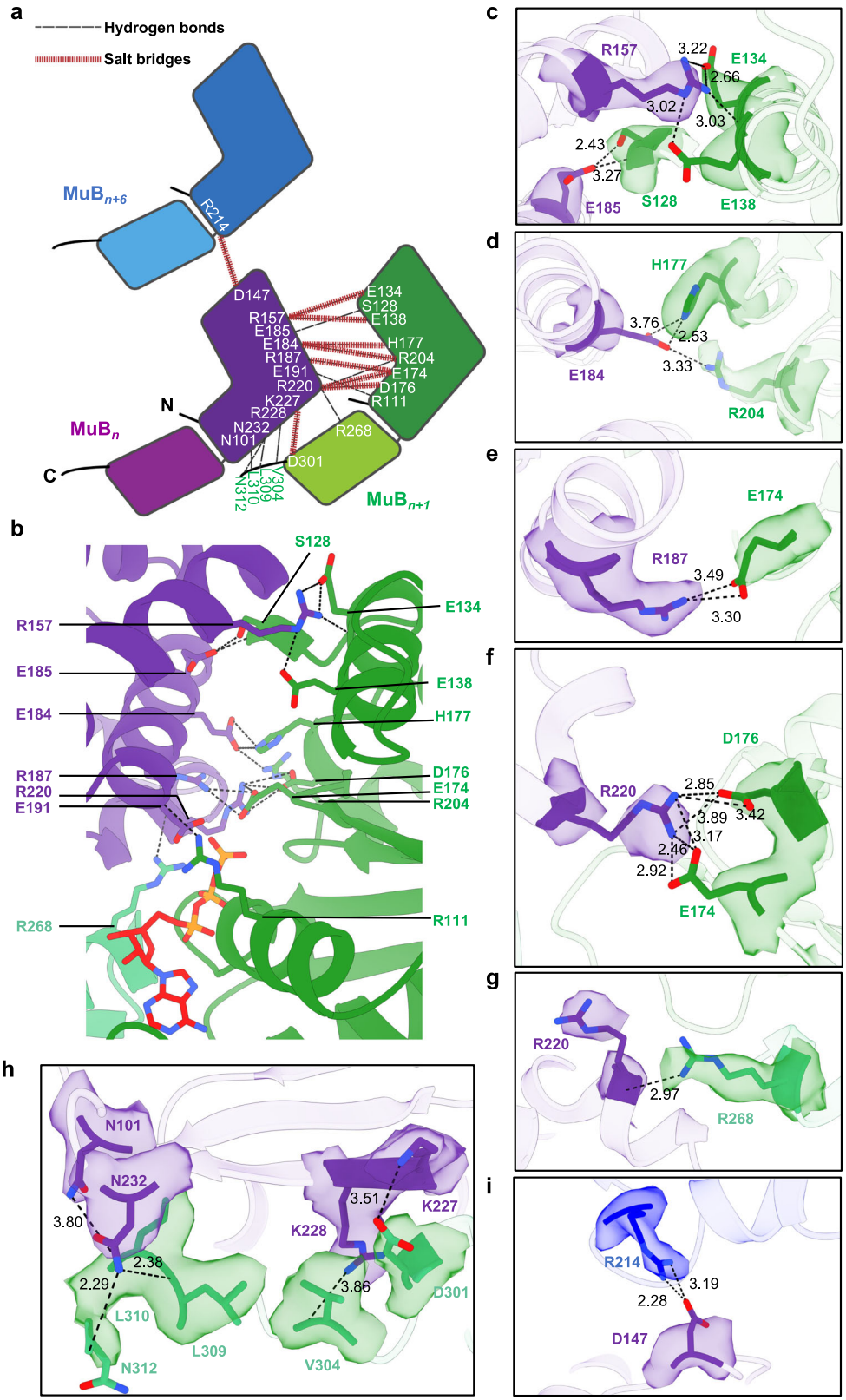

Fig. 3 | Identification of key residues for MuB oligomerization in the ATP(+)-DNA(+)-MuB helical filament. a Representative subunits for the analysis of intermolecular interactions. **b** Hydrogen bonds between MuB$_n$ AAA-α/β and MuB$_{n+1}$ AAA-α/β, AAA-α. **c**–**h** Hydrogen bonds between MuB$_n$ and MuB$_{n+1}$. **i** Hydrogen bonds between the MuB$_n$ and MuB$_{n+6}$. Hydrogen bonds and salt bridges are shown in black and red dashes, respectively. The residues involved in hydrogen bonding are displayed as the map fitted with the model, and the hydrogen bond distances (Å) are indicated.

https://doi.org/10.1038/s41467-024-50722-1

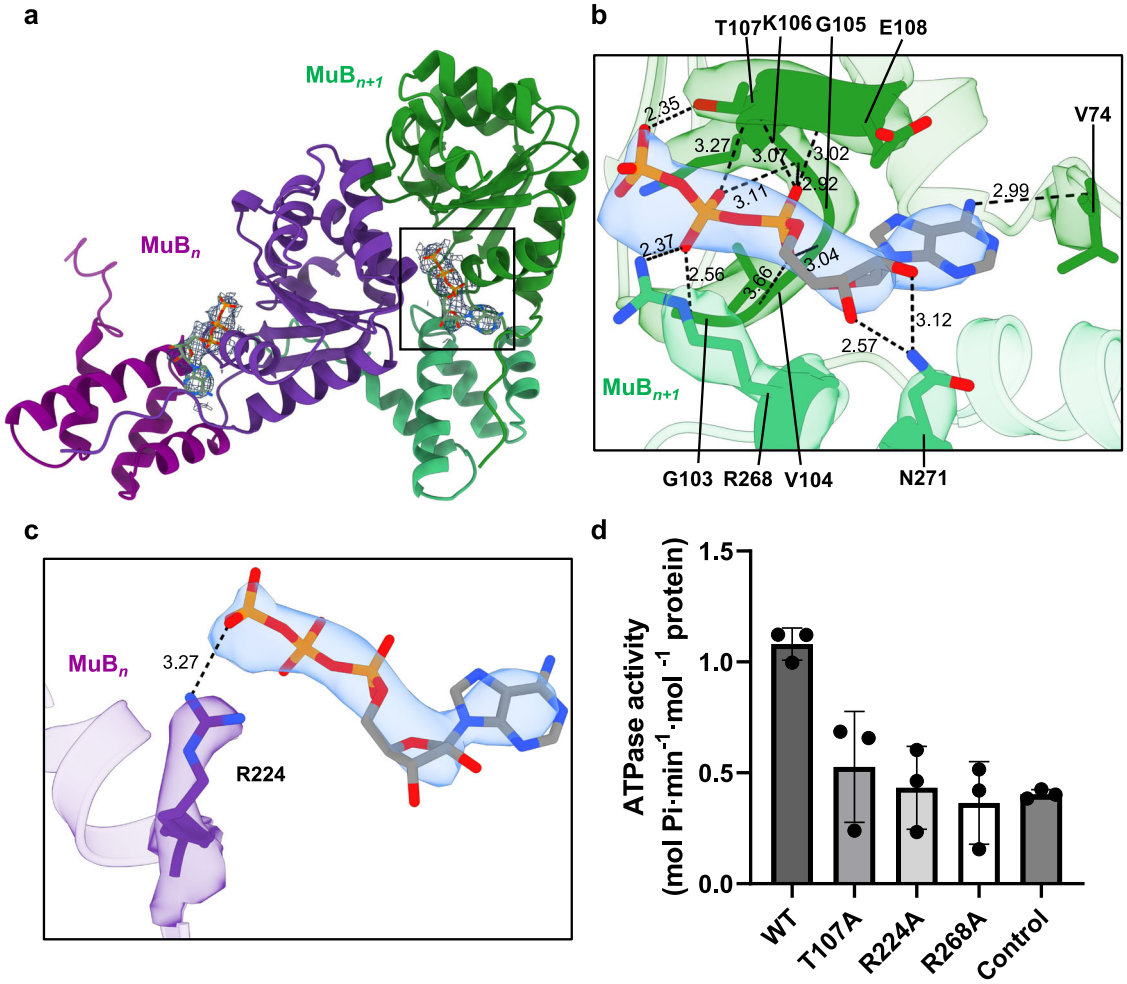

Fig. 4 | MuB-ATP interactions in the ATP(+)-DNA(+)-MuB helical filament. a ATP, situated at the interface between the α/β and α subdomains, has a strong cryo-EM density. **b** Residues that interact with ATP in the same subunit. **c** ATP interacts with the Arginine-finger R224 from the neighboring subunit. Black dashed lines indicate hydrogen bonds. Residues interacting with ATP are shown as the map fitted with the model, and the hydrogen bond distances (Å) are denoted. **d** ATPase activities of wild-type and mutant MuB. WT, wild-type; control, no MuB. Data points are shown as the mean ± SEM (n = 3 independent experiments). Source data are provided as a Source Data file.

MuB mutants with the R150A alteration exhibited a marked decrease in DNA binding compared to the wild-type, and their filament-forming capability was also impaired (Fig. 5e and Supplementary Fig. 5b). Therefore, while residues R150, R151, and K152 in the α/β subdomain all contribute to DNA interactions, R150 plays a pivotal role in DNA engagement. In pioneering work, Mizuno et al. also identified the Sensor-II, Arginine-finger, and the DNA-binding loop by combining sequence analysis, site-directed mutagenesis, and biochemical assays[14]. Our high-resolution cryo-EM structure not only corroborates the presence and functional significance of these essential motifs within MuB but also provides visual confirmation of their spatial arrangement and interaction within the protein. By visualizing these critical elements in the context of the full protein structure, our results enhance the molecular understanding of MuB's mechanism of action, offering a complementary perspective to the biochemical insights provided by Mizuno et al. This synergy between structural and functional analyses highlights the value of integrating diverse methodological approaches to unravel protein function at the molecular level.

Non-unidirectional MuB filamentation may provide a mechanism for locating potential target sites

During the 2D classification of ATP(+)-DNA(+)-MuB filaments, our analysis revealed the presence of two additional distinct classes, each manifesting unique structural characteristics as depicted in Supplementary Fig. 3g. The first of these classes is characterized by a pair of helical filaments converging towards each other, exhibiting opposing polarities. This arrangement stands in contrast to the unidirectional helical filament resolved above (Supplementary Fig. 3b). The second class is distinguished by its composition, consisting exclusively of a double-layered structure.

To gain deeper insights into these unexpected structures, we reprocessed the ATP(+)-DNA(+)-MuB filament data. This reprocessing involved expanding the box size used for analysis, from 336 × 336 pixels to 800 × 800 pixels. The resulting reconstruction unveiled colliding helical filaments characterized by their reversed polarities and the presence of bare DNA (Supplementary Fig. 3c). This unique architectural configuration might be attributable to the initiation of assembly at multiple sites.

Compared to other transposons like Tn7 and Tn7-like systems, Mu transposons exhibit a more random selection of target sites. This randomness can be attributed to the absence of target selection proteins like TnsD/TniQ and TnsE[37–39]. A similar observation of filament collisions was made in the context of the recently characterized Tn7-like transposon, ShCAST[37]. In this system, the stability of the conflicting filaments was found to exceed that of the unidirectional filaments. In addition, the interface between the two TnsC subunits aligns with

https://doi.org/10.1038/s41467-024-50722-1

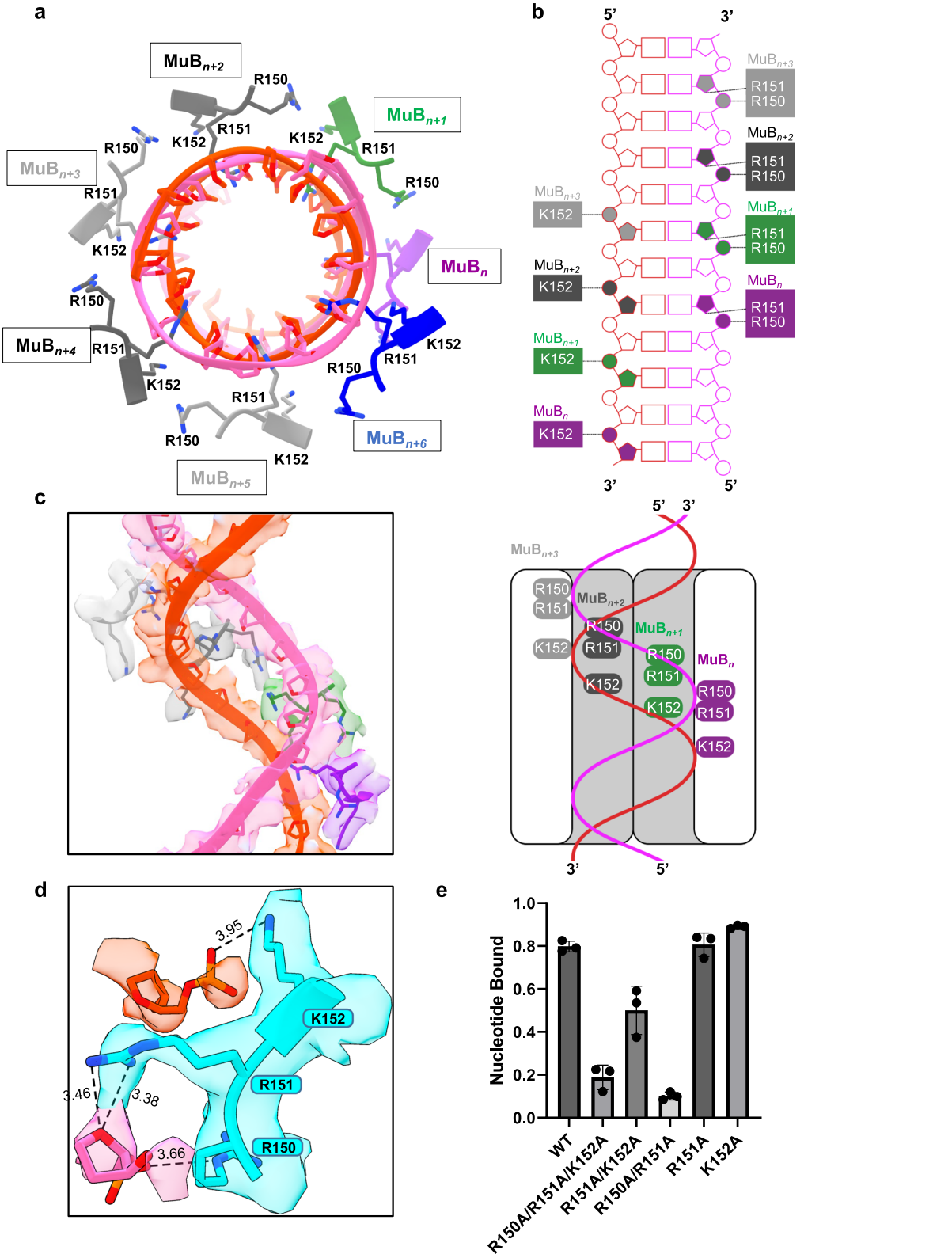

Fig. 5 | Identification of key residues for DNA Binding in the ATP(+)-DNA(+)-MuB helical filament. a Top view of one helical turn with dsDNA and interacting residues shown. **b** Interactions between DNA and MuB's basic residues. **c** Side view of the helical turn with dsDNA and interacting residues shown. **d** Zoom in-view shows the interactions between DNA and the DNA-binding loop, with interaction distances (Å) shown. **e** DNA-binding assay by agarose-EMSA. WT, wild-type. Data points are shown as the mean ± SEM (n = 3 independent experiments). Source data are provided as a Source Data file.

the known TniQ binding site, suggesting a role for TniQ in replacing this interface at the conflicting filaments to delineate the target site[37]. Combined with prior research that established the preference for strand-transfer reactions at DNA sites adjacent to the MuB filament ends[40], it is reasonable to propose that the formation of opposing MuB filaments could serve as a mechanism enabling MuB to identify potential target sites.

According to Mizuuchi et al. [39], Mu transposition shows a marked preference for single-nucleotide mismatches in the DNA. To verify our above hypothesis, we introduced four single mismatches at intervals of 200 bp in the DNA substrate and observed an increase in converging filaments from 2.0% to 12.2%, compared to the wild-type DNA (Supplementary Figs. 3c and 6a–d). In addition, we designed a shorter DNA with central mismatches[38] and noted potential convergences in the middle region (Supplementary Fig. 6e). These observations support our hypothesis that opposing MuB filaments could locate potential target sites for Mu transposition.

ADP-induced DNA(+) MuB structures represent different MuB disassemblies during Mu transposition

In our examination of the class characterized by a bilayer structure (Supplementary Fig. 3g), we speculate that these structures are indicative of a disassembly process of MuB filaments. This hypothesis is supported by the observations that MuB exhibits a relatively low ATPase activity when MuA is absent[13] and polymer disassembly is much slower than assembly[41]. To simulate this disassembly process in vitro, we prepared an ADP(+)-DNA(+)-MuB specimen. Subsequent data processing revealed that ADP-induced DNA(+) MuB forms stacked rings without helical structural features (Supplementary Fig. 7). This structural formation precludes resolution via helical reconstruction. Furthermore, the 2D projection information obtained for this ring-stacked structure is predominantly from the side view, making it unsuitable for analysis using single-particle analysis. Intriguingly, we also observed other classes manifesting either double-ring or triple-ring structures (Supplementary Fig. 7b). To acquire high-resolution structural information on these disassembled intermediates, we reduced the length of DNA from 963 bp to 47 bp, which could increase the prevalence of ring structures (Supplementary Fig. 2).

The 2D classification of the new dataset showed that ADP-induced DNA(+) MuB exists in various oligomeric states, including stacked ring-forming filaments, double rings, and triple rings (Supplementary Fig. 8a, b). During data processing, we encountered challenges in achieving high-resolution structures for the triple-ring and higher-order structures. Consequently, we focused our detailed data processing efforts on the double-ring structures. This strategy led to the identification of two distinct classes, distinguishable by the presence or absence of density within the ring. It is hypothesized that this density may originate from the DNA substrate. The first class, characterized by intra-ring density, exhibits a higher variability, which may be attributed to the high flexibility of the DNA substrate. On the other hand, the second class, lacking intra-ring density, demonstrated a more rigid and stable structure, conducive to achieving finer structural detail (Supplementary Fig. 8c). Cryo-EM reconstructions of the second class unveiled that the double-ring state forms symmetric structures (Fig. 6a and Supplementary Figs. 8–10). These structures can be described as two sets of nonamers or decamers configured in reverse, closely resembling the configuration observed when converging filaments meet (Figs. 6a and 7a–d). The absence of double-ring structures aligned in the same direction further indicates that upon ATP hydrolysis, the reverse configuration we observe is more resistant to disassembly compared with the unidirectional configuration (Fig. 7d). ADP's presence in the nucleotide-binding pocket is marked by strong cryo-EM density, as observed in Fig. 6b and Supplementary Fig. 10. Altered intersubunit interactions, especially the lack of intersubunit contacts in the nucleotide-binding pocket, lead to these different MuB subunit organizations and higher conformational flexibilities (Fig. 6b and Supplementary Figs. 8, 11, 12). These conformations have enlarged diameters, possibly facilitating their disengagement from DNA substrates (Fig. 6a). Moreover, MuA promotes the formation of ring structures (Supplementary Fig. 13).

Based on the molecular insights provided by our electron microscopy structures and biochemical results, we propose a mechanistic model to explain how MuB assembles and disassembles on DNA targets to promote Mu transposition (Fig. 7e). Upon ATP binding, MuB forms helical filaments on DNA. This assembly occurs at multiple sites, especially around the single-mismatch, not only increasing the likelihood of filament convergence with opposite polarities but also strategically exposing DNA target sites, making them accessible to MuA. In this context, MuA's role is twofold: it captures these exposed DNA regions at the interface of converging MuB filaments and stimulates ATP hydrolysis within MuB. The stimulation of ATP hydrolysis by MuA likely involves direct protein-protein interactions[42], which are pivotal for initiating the disassembly of MuB filaments and subsequent formation of ring structures with larger diameters (Fig. 6 and Supplementary Fig. 13). Notably, our observations revealed no significant conformational changes between ATP- and ADP-bound states of MuB monomers (RMSD = ~ 0.7 Å), suggesting that MuA's stimulation of ATP hydrolysis might operate through mechanisms that do not involve direct conformational alterations in MuB during the ATP to ADP transition. As a result of these processes, MuB eventually detaches from the DNA, paving the way for the exposure of larger regions of naked DNA, essential for the transposition process. Besides, this dynamic interplay between MuB filament assembly and disassembly, modulated by MuA, offers insights into the structural basis of transposition immunity. Transposition immunity ensures that DNA sequences already occupied by transposons are not targeted again, maintaining genomic integrity[15–17]. Our structural model suggests that the specific arrangements of MuB filaments and their regulated disassembly by MuA could contribute to this immunity, preventing repeated insertions into the same DNA regions and favoring novel insertion locations. Taken together, our proposed model offers an insightful mechanism into the role of MuB in target DNA capture and Mu transposition.

Discussion

MuB is an AAA+ protein that plays a crucial role in the DNA transposition process of bacteriophage Mu, a mechanism that allows for the movement of DNA sequences within a genome[16]. Past research emphasizes the pivotal role MuB filaments play in the target DNA selection for the Mu transposition. However, a more profound understanding of the filament structure and the complexities of the MuB polymer assembly and disassembly mechanisms remains to be elucidated.

Our structural characterization of MuB has unveiled some unexpected findings. The MuB-ATP assemblies, initially challenging to characterize due to their poor solubility, have been identified in various oligomeric states. These states potentially represent different phases of MuB during the transposition process. Significantly, the 3.4-Å structure of the ATP(+)-DNA(+)-MuB helical filament represents, to our knowledge, the first high-resolution structure of MuB. It allows us to obtain the atomic model of the MuB protomer, and to further reveal the mechanism by which MuB assembles into filaments on DNA. Although typically, the NTD of MuB folds into four compact α-helices with a characteristic HTH motif, a common feature of DNA-binding domains[25], it is absent in our cryo-EM map. Our structure instead shows its deviation from the axial channel of the filament, implying that the NTD does not directly participate in DNA binding (Supplementary Fig. 14). Moreover, despite previous assumptions about the NTD's role in favoring filament-filament interactions[25], our findings did not observe such interactions. Therefore, the role of MuB's NTD warrants further investigation.

https://doi.org/10.1038/s41467-024-50722-1

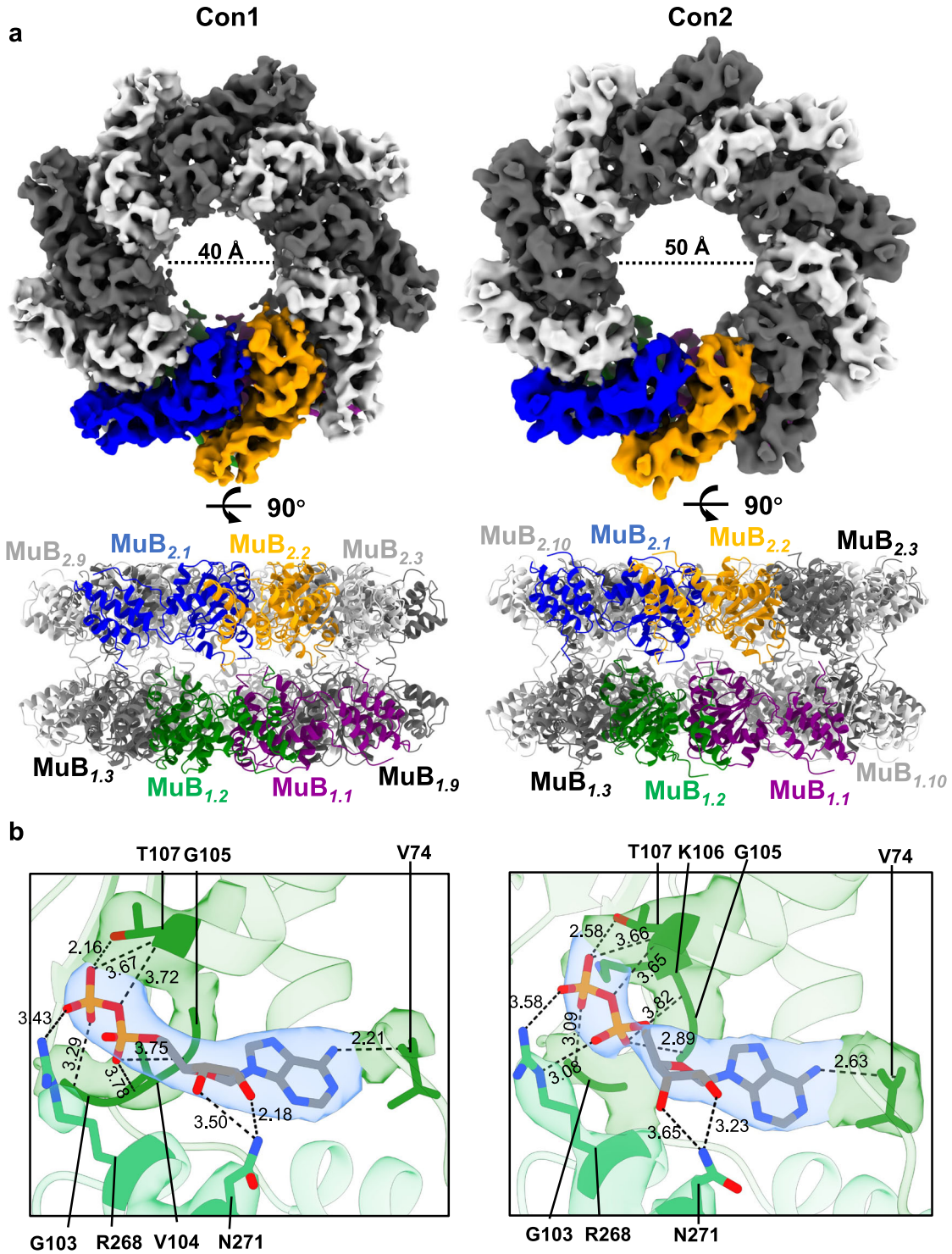

Fig. 6 | Two representative conformations obtained from the ADP(+)-DNA(47 bp +)-MuB specimen. a Cryo-EM maps and atomic models of the ADP(+)-DNA(47 bp +)-MuB conformations 1 and 2. Conformation 1 (Con1) was applied with D9 symmetry, and Conformation 2 (Con2) was applied with D10 symmetry. **b** Residues that interact with ADP. The AAA-α/β and AAA-α subdomains are shown as forest green and medium sea green, respectively. Black dashed lines indicate hydrogen bonds. Residues interacting with ADP are shown as the map fitted with the model, and the hydrogen bond distances (Å) are denoted.

In addition to studying the MuB-ATP assemblies, our research also explored the MuB-ADP assemblies, together revealing a range of oligomeric structures. These include filaments with reverse polarities and bare DNA, stacked ring-forming filaments lacking helical features, and double- and triple-ring structures. This variety illustrates the dynamic assembly and disassembly process of MuB, where individual molecules continuously join and dissociate from the filament[27,28]. This dynamic nature is believed to be crucial for the ability of MuB to search for and select the target DNA for transposition[41]. The diversity of these structures provides a direct structural explanation for previous biochemical analysis that shows rapid assembly and slow disassembly of MuB polymers[41].

Emerging from our electron microscopy structures and biochemical findings, we propose a mechanistic model of the MuB-mediated

https://doi.org/10.1038/s41467-024-50722-1

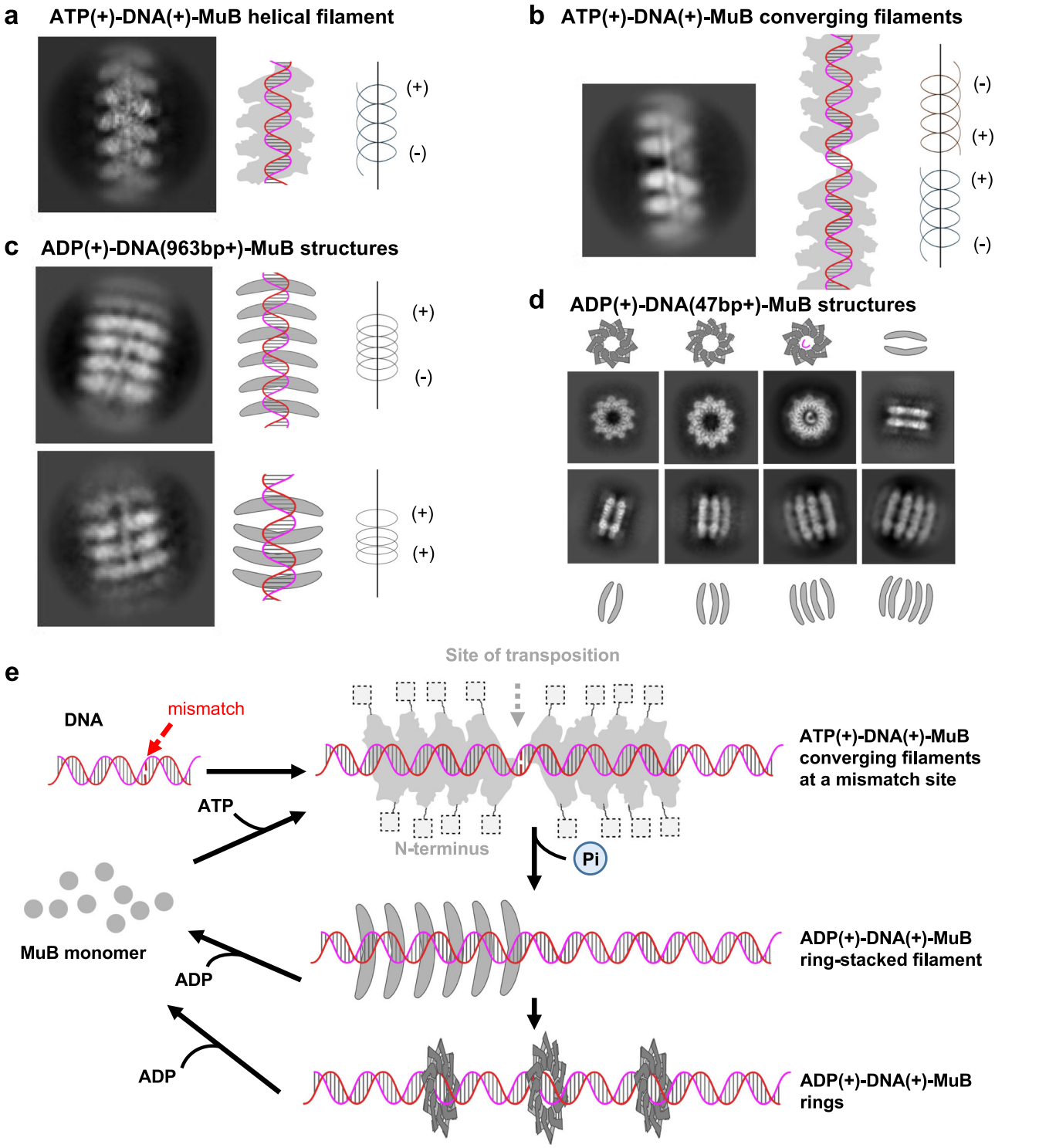

Fig. 7 | Architectural dynamics of MuB filaments during Mu transposition. **a** Representative 2D class average and cartoon of the ATP(+)-DNA(+)-MuB helical filament. **b** Representative 2D class average and cartoon of the ATP(+)-DNA(+)-MuB converging filaments with reverse polarities. **c** Representative 2D class averages and cartoons of the ADP(+)-DNA(+)-MuB structures. The DNA substrate was 963 bp. **d** Representative 2D class averages and cartoons of the ADP(+)-DNA(+)-MuB structures. The DNA substrate was 47 bp. **e** Proposed Model for MuB behaviors in Mu transposition.

transposition process, heavily contingent on the ATPase activity of MuB. This model is simplified into the following stages: (1) ATP binding and filament formation, whereby ATP binds to MuB's AAA+ module, facilitating DNA binding and filament formation[41]; (2) target DNA selection, where opposing helical filaments expose potential target sites, enabling the recruitment of the MuA transposase to initiate transposition[43]; and (3) ATP hydrolysis and filament disassembly, where ATP hydrolysis by the AAA+ module leads to altered intersubunit interactions and subsequent filament disassembly, with several disassembly intermediate states observed in our study (Supplementary Fig. 8). This disassembly is thought to be necessary for the completion of the transposition process[14,40].

In comparing the structural and functional insights from our current study with those of Mizuno et al. [14] regarding MuB, both

studies utilize cryo-EM for structural analysis, with our study enhancing the resolution further to obtain a 3.4-Å resolution of the MuB filament and identify additional oligomeric states of MuB. While Mizuno et al. emphasized MuB's role in DNA binding and manipulation during transposition, our research builds on this by elucidating specific interactions within MuB oligomers, their implications for ATP and DNA binding, and extending understanding by describing various oligomeric states, offering an intriguingly mechanistic model that converging filaments would expose DNA target sites for MuA. This comparative analysis highlights advancements in understanding MuB's complex role in bacterial DNA transposition, illustrating both continuity and evolution in scientific insights over the past decade (Supplementary Fig. 15).

Our current observations on MuB structures provide a solid foundation for future research directions aimed at unraveling the MuB-MuA interaction and its role in bacteriophage Mu DNA transposition. Potential avenues include employing co-immunoprecipitation and cryo-EM to visualize the MuB-MuA complex, identifying key interaction sites through mutagenesis and functional assays, and exploring the regulatory mechanisms influencing this interaction. In addition, investigating how MuA stimulates MuB's ATPase activity, possibly through mechanisms beyond simple structural alterations in MuB upon nucleotide exchange, could offer valuable insights. These studies will not only clarify the molecular dynamics between MuB and MuA but also enhance our understanding of their coordinated function in DNA transposition, paving the way for novel applications in genetic engineering and therapy.

Methods

Cloning and mutagenesis

The plasmids pET14b-wild-type codon-optimized MuB (wtMuB) and MuA (wtMuA) were used to express the 6 × His tagged fusion proteins with a thrombin cleavage site between the His-tag and the protein sequence. The MuB mutants were PCR-amplified using mutant-specific primers with overlapping sequences from the plasmid pET14b-wtMuB and recombined using the ClonExpress II One Step Cloning Kit (Vazyme). The codon-optimized protein sequences and mutagenic primers are listed in Supplementary Data 1.

Protein expression and purification

Rosetta(DE3)pLysS *Escherichia coli* cells transformed with the pET14b-wtMuB or pET14b-wtMuA plasmid were grown at 37 °C in 2 L of LB medium with 0.1 mg/mL ampicillin to an optical density at 600 nm of 0.6 ~ 0.8, and protein expression was induced by the addition of 0.8 mM isopropyl β-D-1-thiogalactopyranoside (IPTG) at 16 °C overnight. Cells were collected by centrifugation resuspended in 40 mL lysis buffer [20 mM Tris pH 7.8, 1 M NaCl, 1 mM dithiothreitol (DTT), 0.2 mM Phenylmethanesulfonyl fluoride (PMSF), 10% Glycerol] and disrupted by sonication. The cell lysate was clarified by centrifugation at 4 °C at 14,000 × *g* for 1 h. The supernatant was loaded onto Ni-NTA resin (Qiagen). After column washing with 20 mL of lysis Buffer plus 30 mM imidazole, the protein was eluted in lysis buffer plus 0.3 M imidazole. The eluted sample was concentrated to ~ 7 mg/mL using an Amicon Ultra Centrifugal filter (30 kDa MWCO, EMD Millipore). Human thrombin (Biosharp) was added to the concentrated sample at a final concentration of 0.05 μ/μL and incubated on ice overnight. 500 μL of the His-tag cleavaged sample was loaded to size-exclusion chromatography (AKTAgo, Cytiva) using a Superdex 75 (for MuB) or Superose 6 (for MuA) Increase 10/300 GL sizing columns (Cytiva) equilibrated with storage buffer (20 mM Tris pH7.8, 0.6 M KCl, 1 mM DTT, 4% Glycerol). The MuB peak corresponding to fractions 10.46 mL to 11.95 mL and the MuA peak corresponding to fractions 15.80 mL to 17.30 mL were collected and stored at − 80 °C. All of the Buffers above were kept at 4 °C to prevent aggregated precipitation of MuB. The expression and purification of the MuB mutants were performed as for wtMuB.

Grid preparation and data acquisition for negative-staining electron microscopy

The 963 bp DNA was amplified by PCR using the plasmid pET14b-wtMuB as the template, while the 47 bp DNA with or without central mismatches was prepared by annealing two 47-nt oligonucleotides. The 963 bp DNA with four single mismatches was amplified as described in the previous study[39]. Briefly, the wild-type 963 bp DNA was obtained by PCR from pET14b-wtMuB, and mutant 963 bp DNA was amplified from the pET14b-MuB mutant containing four single mutations spaced 200 bp apart. The wild-type and mutant 963 bp DNA samples were mixed in a 1:1 ratio and used as PCR templates to amplify to the plateau phase, thereby generating mismatched DNA (Supplementary Data 1 and Supplementary Table 1).

Complexes of MuB with DNA and ATP were prepared by gently stirring 5 μL MuB (~ 1.51 mg/mL), 1 μL 963 bp DNA (~ 180 ng/μL), 3 μL 20 mM Tris (pH 7.8), and 1 μL 10 × T4 DNA Ligase Reaction Buffer (NEB, 500 mM Tris-HCl, 100 mM $MgCl_2$, 10 mM ATP, 100 mM DTT, pH 7.5), followed by incubation for 5 min on ice and 5 min at room temperature (RT). Then 3 μL sample was applied to glow-discharged 200-mesh copper grids with a continuous layer of thin carbon coated. The excess sample was removed by blotting, and the grids were then stained with 4 μL 1% (wt/vol) uranyl acetate, followed by two washes in 4 μL droplets of 1% (wt/vol) uranyl acetate. Excess stain was blotted away, and grids were air-dried. The grids were subsequently imaged using a Tecnai F20 electron microscope, operated at 200 kV. Images were recorded using a nominal magnification of 62,000 with a calibrated pixel size of 1.81 Å. The same protocol was followed for the preparation and imaging of other MuB complexes.

Cryo-EM grid preparation and data collection

The ATP(+)-DNA(+)-MuB specimen was prepared by gently stirring 5 μL MuB (~ 1.51 mg/mL), 1 μL 963 bp DNA (~ 180 ng/μL), 3 μL 20 mM Tris (pH 7.8), and 1 μL 10 × T4 DNA Ligase Reaction Buffer and incubated for 5 min on ice plus 5 min at RT. For datasets 1 and 3 (Supplementary Table 2), 3 μL samples were applied onto glow-discharged 200-mesh R1.2/1.3 Quantifoil copper grids. The grids were blotted for 3.5 s and 4.5 s, respectively, and rapidly cryo-cooled in liquid ethane using a Vitrobot Mark IV (Thermo Fisher Scientific) at 4 °C and 100% humidity. For dataset 2 (Supplementary Table 2), 3 μL samples were applied onto glow-discharged 200-mesh R2/1 (+ 2 nm carbon) Quantifoil copper grids and blotted for 1 s. The grids were screened using a Glacios cryo-electron microscope (Thermo Fisher Scientific) operated at 200 kV. Then they were imaged in a Titan Krios cryo-electron microscope (Thermo Fisher Scientific) operated at 300 kV at a magnification of 105,000 × (corresponding to a calibrated sampling of 0.82 Å per pixel). Micrographs were recorded by EPU software (Thermo Fisher Scientific, version 2.7) with a Gatan K3 Summit direct electron detector, where each image was composed of 30 individual frames with an exposure time of 3 s and a dose rate of 20.3 electrons per second per $Å^2$. Finally, a total of 6298 movie stacks were collected with a defocus range of − 2.0 to − 3.0 μm.

The ATP(+)-DNA(+ mismatch)-MuB specimen was prepared by gently stirring 5 μL MuB (~ 2.29 mg/mL), 1 μL 963 bp DNA with four single mismatches (~ 353.3 ng/μL), 3 μL 20 mM Tris (pH 7.8), and 1 μL 10 × T4 DNA Ligase Reaction Buffer and incubated for 5 min on ice plus 5 min at RT. Then 3 μL samples were applied onto glow-discharged 200-mesh R1.2/1.3 Quantifoil copper grids and blotted for 5 s. The grids were screened and imaged using the Glacios cryo-electron microscope with a magnification of 120,000 × (corresponding to a calibrated sampling of 1.2 Å per pixel). Micrographs were recorded by the EPU software with a Falcon3 direct electron detector, where each

image was composed of 32 individual frames with an exposure time of 2 s and a dose rate of 22.1 electrons per second per Å^2. Finally, a total of 412 movie stacks were collected with a defocus range of −1.5 to −2.9 µm.

The ADP(+)-DNA(+)-MuB specimen was prepared by gently stirring 5 µL MuB (~1.6 mg/mL), 4 µL 963 bp DNA(~149 ng/µL), and 1 µL 10 mM ADP Buffer (20 mM Tris, 10 mM ADP, 100 mM $MgCl_2$, 100 mM DTT, pH 7.8) and incubated for 5 min on ice plus 5 min at RT. 3 µL samples were applied onto glow-discharged 200-mesh R1.2/1.3 Quantifoil copper grids and blotted for 4.5 s. The grids were screened and imaged on the Glacios cryo-electron microscope with a magnification of 120,000 × (corresponding to a calibrated sampling of 1.2 Å per pixel). Micrographs were recorded by the EPU software, where each image was composed of 32 individual frames with an exposure time of 2 s and a dose rate of 23 electrons per second per Å^2. Finally, a total of 329 movie stacks were collected with a defocus range of −2.0 to −3.0 µm.

Besides, another ADP(+)-DNA(+)-MuB specimen with a shorter DNA substrate (47 bp) was also prepared by gently stirring 5 µL MuB (~2.01 mg/mL), 4 µL 47 bp DNA (5 µM), and 1 µL 10 mM ADP Buffer and incubated for 5 min on ice plus 5 min at RT. 3 µL samples were applied onto glow-discharged and polylysine-pretreated 200-mesh R2/1 (+2 nm carbon) Quantifoil copper grids, followed by blotting for 1 s. The grids were screened using the Glacios cryo-electron microscope. Then they were imaged in the Titan Krios cryo-electron microscope at a magnification of 105,000 × (corresponding to a calibrated sampling of 0.82 Å per pixel). Micrographs were recorded by the EPU software, where each image was composed of 30 individual frames with an exposure time of 3 s and a dose rate of 15.6 electrons per second per Å^2. Finally, a total of 9510 movie stacks were collected with a defocus range of −2.0 to −3.0 µm. The details for data collection are listed in Supplementary Tables 2–5.

Cryo-EM data processing

Data processing was performed using the software packages cryoSPARC[29], EMAN2[44], and Relion[45]. Micrographs were motion corrected with patch motion correction. The CTF parameters of micrographs were estimated using patch CTF estimation or CTFFIND4[46]. For the ATP(+-DNA(+)-MuB helical filament, the diameter for the filament tracer was set to 150 Å with a separation distance of 0.2 between segments. After inspecting particle picks and a few rounds of 2D classification, 377,689 particles were selected for further processing. The helical parameters (rise and twist) were searched using the "Symmetry Search Utility" option in cryoSPARC. For structure determination, we applied an initial helical parameter of 56° of helical twist and a 7-Å helical rise per subunit using helical refinement in cryoSPARC, and these parameters were later refined to 56.156° and 6.913 Å, respectively. The final volume after 3D refinement displayed clear α-helices and achieved a resolution of 3.4 Å as estimated by Fourier shell correlation. For the ATP(+)-DNA(+)-MuB converging filaments, 67,543 particles were selected after 2D classification for further heterogeneous refinement using the template map generated using the "Ab initio reconstruction" option in cryoSPARC. Finally, a class with 12,317 particles from heterogeneous refinement represented the converging filaments. The workflow described here is depicted in Supplementary Fig. 3.

For the ATP(+)-DNA(963 bp + mismatch)-MuB specimen, 70,022 particles were selected after blob-picking and 2D classification. A total of 25,891 particles of converging filaments were subjected to heterogeneous refinement with the template derived from the Ab initio reconstruction of 5413 particles of representative converging filament 2D averages. Finally, a class with 8524 particles represented the converging filaments. The workflow described here is depicted in Supplementary Fig. 6.

For the ADP(+)-DNA(963 bp +)-MuB specimen, 8320 particles were selected after manual picking, template-picking, and 2D classification. The workflow described here is depicted in Supplementary Fig. 7.

For the ADP(+)-DNA(47 bp +)-MuB specimen, 9367 micrographs were selected after patch motion correction in cryoSPARC and CTF estimation by CTFFIND4. All particles were auto picked using the NeuralNet option in EMAN2 and further checked manually. The resulting number of boxed particles was 2,587,451. Then, particle coordinates were imported to Relion, where 2D classification was performed to remove 2D class averages with less resolved features. The selected 2,405,875 particles were subjected to 3D classification and two good classes were derived, distinguished by the presence or absence of density within the ring. After another round of 2D classification, heterogeneous refinements were performed to achieve more classes, followed by non-uniform refinement. To be noted, for the classes (Con1 and Con2) without density inside the ring, the symmetries D9 and D10 were imposed, while no symmetries were imposed for the classes (Con1 and Con2) with density inside the ring, due to their flexibilities. The symmetry expansion and local refinement were further applied on Con1 and Con2 for generating higher-resolution single-subunit maps. The workflow described here is depicted in Supplementary Fig. 8. The FSC curves representing the resolutions for these conformations are shown in Supplementary Fig. 9.

Model building and refinement

Model building was first performed on the ATP(+)-DNA(+)-MuB helical filament. The full-length sequence of MuB was imported into the AlphaFold2 server[47] for the initial model generation of the protomer. The initial models of protomers were rigidly fitted into the cryo-EM map, and then molecular dynamics flexible fitting (MDFF)[48] was applied to flexibly fit the atomic model into the map, followed by optimization with Coot[49] and Phenix.real_space_refine[50]. The bound ATP and DNA were generated using Chimera[51], manually adjusted by Coot, and refined by Phenix.real_space_refine. The final model was evaluated by MolProbity[52] and Q-score[53].

For the model building of the octadecamer from the ADP(+)-DNA(47 bp +)-MuB specimen, the protomer from the ATP(+)-DNA(+)-MuB helical filament was first rigidly fitted into the protomer cryo-EM map of the octadecamer from symmetry expansion. Then Coot and Phenix.real_space_refine were conducted. The bound ADP was generated using Coot and refined by Phenix.real_space_refine. The resulting models of protomers were rigidly fitted into the cryo-EM map of the ADP(+)-DNA(47 bp +)-MuB octadecamer (conformation 1) and refined using phenix.real_space_refine. The final model was evaluated by MolProbity[52] and Q-score[53]. Similar procedures were performed for the model building of the twenties from the ADP(+)-DNA(47 bp +)-MuB sample (conformation 2). Statistics of the model building are summarized in Supplementary Tables 2 and 5. All figures were prepared using Chimera[51] and ChimeraX[54].

ATPase activity assays

ATPase assays were carried out as previously described[55]. Briefly, reactions were performed at RT for 30 min in a 75 µl system containing 2 µM MuB (or the mutants), 20 mM Tris·HCl (pH 7.8), 0.15 M KCl, 10 mM $MgCl_2$, 20% (vol/vol) glycerol, 10 mM DTT, 0.1 mg/mL BSA, 2 µM 47 bp DNA, and 2 mM ATP. Then 8.25 µL aliquots of 0.2 M EDTA were used to stop the reaction. Reaction products were quantified using an Infinite E Plex (TECAN) at OD630. Data were analyzed with Prism 8.3.0.

DNA electrophoretic mobility shift assay (EMSA)

EMSA-Agarose assay was carried out essentially as described[56,57]. Briefly, 10 µL samples of 6.36 µM MuB (or the mutants) and 0.25 µM 5′-

FAM labeled 47 bp DNA in 20 mM Tris·HCl (pH 7.8), 0.3 M KCl, 2% (vol/vol) glycerol, and 10 mM $MgCl_2$ were incubated with 2 mM ATP for 5 min at 4 °C, applied to 2% Agarose, quantified using an ImageQuant LAS 4000 (Cytiva) and measured by ImageJ[58]. The DNA sequence was the same as that used in the ATPase activity assay to test the effect on nucleotide binding.

Statistics and reproducibility

Sample sizes are described in the legends. No statistical method was used to predetermine the sample size. Quantitative experiments were typically repeated in technical triplicate, demonstrating reproducibility.

Reporting summary

Further information on research design is available in the Nature Portfolio Reporting Summary linked to this article.

Data availability

Cryo-EM structures and atomic models generated in this study have been deposited in the wwPDB OneDep System under EMD accession codes EMD-38695, EMD-38696, EMD38697, EMD-38698, EMD-38699, and PDB ID codes under accession codes 8XVB, 8XVC, 8XVD, respectively. Source data are provided with this paper.

References

1. Sandulache, R., Prehm, P. & Kamp, D. Cell wall receptor for bacteriophage Mu G(+). *J. Bacteriol.* **160**, 299–303 (1984).
2. Taylor, A. L. Bacteriophage-induced mutation in Escherichia coli. *Proc. Natl. Acad. Sci. USA* **50**, 1043–1051 (1963).
3. Harshey, R. M. The Mu story: how a maverick phage moved the field forward. *Mob. DNA* **3**, 21 (2012).
4. Harper, D. R. *Bacteriophages Biology, Technology, Therapy*. (Springer International Publishing, Switzerland, 2021).
5. Walker, M. W. G., Klompe, S. E., Zhang, D. J. & Sternberg, S. H. Novel molecular requirements for CRISPR RNA-guided transposition. *Nucleic Acids Res.* **51**, 4519–4535 (2023).
6. Maertens, G. N., Engelman, A. N. & Cherepanov, P. Structure and function of retroviral integrase. *Nat. Rev. Microbiol.* **20**, 20–34 (2022).
7. Park, J.-U., Tsai, A. W.-L., Chen, T. H., Peters, J. E. & Kellogg, E. H. Mechanistic details of CRISPR-associated transposon recruitment and integration revealed by cryo-EM. *Proc. Natl. Acad. Sci. USA* **119**, e2202590119 (2022).
8. Mizuuchi, M., Baker, T. A. & Mizuuchi, K. Assembly of phage Mu transpososomes: cooperative transitions assisted by protein and DNA scaffolds. *Cell* **83**, 375–385 (1995).
9. Mizuuchi, K. Transpositional recombination: mechanistic insights from studies of mu and other elements. *Annu. Rev. Biochem.* **61**, 1011–1051 (1992).
10. Surette, M. G., Buch, S. J. & Chaconas, G. Transpososomes: stable protein-DNA complexes involved in the in vitro transposition of bacteriophage Mu DNA. *Cell* **49**, 253–262 (1987).
11. Craigie, R. & Mizuuchi, K. Transposition of Mu DNA: joining of Mu to target DNA can be uncoupled from cleavage at the ends of Mu. *Cell* **51**, 493–501 (1987).
12. Baker, T. A., Mizuuchi, M. & Mizuuchi, K. MuB protein allosterically activates strand transfer by the transposase of phage Mu. *Cell* **65**, 1003–1013 (1991).
13. Maxwell, A., Craigie, R. & Mizuuchi, K. B protein of bacteriophage mu is an ATPase that preferentially stimulates intermolecular DNA strand transfer. *Proc. Natl. Acad. Sci. USA* **84**, 699–703 (1987).
14. Mizuno, N. et al. MuB is an AAA+ ATPase that forms helical filaments to control target selection for DNA transposition. *Proc. Natl. Acad. Sci. USA* **110**, E2441–E2450 (2013).
15. Adzuma, K. & Mizuuchi, K. Interaction of proteins located at a distance along DNA: mechanism of target immunity in the Mu DNA strand-transfer reaction. *Cell* **57**, 41–47 (1989).
16. Walker, D. M. & Harshey, R. M. Deep sequencing reveals new roles for MuB in transposition immunity and target-capture, and redefines the insular Ter region of. *Mob. DNA* **11**, 26 (2020).
17. Adzuma, K. & Mizuuchi, K. Target immunity of Mu transposition reflects a differential distribution of Mu B protein. *Cell* **53**, 257–266 (1988).
18. Jang, S., Sandler, S. J. & Harshey, R. M. Mu insertions are repaired by the double-strand break repair pathway of Escherichia coli. *PLoS Genet.* **8**, e1002642 (2012).
19. Choi, W. & Harshey, R. M. DNA repair by the cryptic endonuclease activity of Mu transposase. *Proc. Natl. Acad. Sci. USA* **107**, 10014–10019 (2010).
20. Abdelhakim, A. H., Sauer, R. T. & Baker, T. A. The AAA+ ClpX machine unfolds a keystone subunit to remodel the Mu transpososome. *Proc. Natl. Acad. Sci. USA* **107**, 2437–2442 (2010).
21. Bhattacharyya, S. et al. Phage Mu Gam protein promotes NHEJ in concert with ligase. *Proc. Natl. Acad. Sci. USA* **115**, E11614–E11622 (2018).
22. Chamblee, J. S. et al. Endolysin regulation in phage Mu Lysis. *MBio* **13**, e0081322 (2022).
23. Harshey, R. M. & Bukhari, A. I. Infecting bacteriophage mu DNA forms a circular DNA-protein complex. *J. Mol. Biol.* **167**, 427–441 (1983).
24. Puspurs, A. H., Trun, N. J. & Reeve, J. N. Bacteriophage Mu DNA circularizes following infection of Escherichia coli. *EMBO J.* **2**, 345–352 (1983).
25. Dramićanin, M., López-Méndez, B., Boskovic, J., Campos-Olivas, R. & Ramón-Maiques, S. The N-terminal domain of MuB protein has striking structural similarity to DNA-binding domains and mediates MuB filament-filament interactions. *J. Struct. Biol.* **191**, 100–111 (2015).
26. Hung, L. H., Chaconas, G. & Shaw, G. S. The solution structure of the C-terminal domain of the Mu B transposition protein. *EMBO J.* **19**, 5625–5634 (2000).
27. Greene, E. C. & Mizuuchi, K. Direct observation of single MuB polymers: evidence for a DNA-dependent conformational change for generating an active target complex. *Mol. Cell* **9**, 1079–1089 (2002).
28. Greene, E. C. & Mizuuchi, K. Visualizing the assembly and disassembly mechanisms of the MuB transposition targeting complex. *J. Biol. Chem.* **279**, 16736–16743 (2004).
29. Punjani, A., Rubinstein, J. L., Fleet, D. J. & Brubaker, M. A. cryoSPARC: algorithms for rapid unsupervised cryo-EM structure determination. *Nat. Methods* **14**, 290–296 (2017).
30. Arinkin, V., Smyshlyaev, G. & Barabas, O. Jump ahead with a twist: DNA acrobatics drive transposition forward. *Curr. Opin. Struct. Biol.* **59**, 168–177 (2019).
31. Miller, J. M. & Enemark, E. J. Fundamental characteristics of AAA+ protein family structure and function. *Archaea* **2016**, 9294307 (2016).
32. Laskowski, R. A., Jabłońska, J., Pravda, L., Vařeková, R. S. & Thornton, J. M. PDBsum: Structural summaries of PDB entries. *Protein Sci.* **27**, 129–134 (2018).
33. Li, S. et al. Molecular basis for ATPase-powered substrate translocation by the Lon AAA+ protease. *J. Biol. Chem.* **297**, 101239 (2021).
34. Li, S. et al. Complete three-dimensional structures of the Lon protease translocating a protein substrate. *Sci. Adv.* **7**, eabj7835 (2021).
35. Li, S. et al. Processive cleavage of substrate at individual proteolytic active sites of the Lon protease complex. *Sci. Adv.* **7**, eabj9537 (2021).
36. Li, S. et al. A 5+1 assemble-to-activate mechanism of the Lon proteolytic machine. *Nat. Commun.* **14**, 7340 (2023).
37. Park, J.-U. et al. Structural basis for target site selection in RNA-guided DNA transposition systems. *Science* **373**, 768–774 (2021).
38. Shen, Y. et al. Structural basis for DNA targeting by the Tn7 transposon. *Nat. Struct. Mol. Biol.* **29**, 143–151 (2022).

39. Yanagihara, K. & Mizuuchi, K. Mismatch-targeted transposition of Mu: a new strategy to map genetic polymorphism. *Proc. Natl. Acad. Sci. USA* **99**, 11317–11321 (2002).
40. Dramićanin, M. & Ramón-Maiques, S. MuB gives a new twist to target DNA selection. *Mob. Genet. Elem.* **3**, e27515 (2013).
41. Greene, E. C. & Mizuuchi, K. Dynamics of a protein polymer: the assembly and disassembly pathways of the MuB transposition target complex. *EMBO J.* **21**, 1477–1486 (2002).
42. Abdelhakim, A. H., Oakes, E. C., Sauer, R. T. & Baker, T. A. Unique contacts direct high-priority recognition of the tetrameric Mu transposase-DNA complex by the AAA+ unfoldase ClpX. *Mol. Cell* **30**, 39–50 (2008).
43. Lemberg, K. M., Schweidenback, C. T. H. & Baker, T. A. The dynamic Mu transpososome: MuB activation prevents disintegration. *J. Mol. Biol.* **374**, 1158–1171 (2007).
44. Tang, G. et al. EMAN2: an extensible image processing suite for electron microscopy. *J. Struct. Biol.* **157**, 38–46 (2007).
45. Scheres, S. H. W. RELION: implementation of a Bayesian approach to cryo-EM structure determination. *J. Struct. Biol.* **180**, 519–530 (2012).
46. Rohou, A. & Grigorieff, N. CTFFIND4: Fast and accurate defocus estimation from electron micrographs. *J. Struct. Biol.* **192**, 216–221 (2015).
47. Mirdita, M. et al. ColabFold: making protein folding accessible to all. *Nat. Methods* **19**, 679–682 (2022).
48. Trabuco, L. G., Villa, E., Mitra, K., Frank, J. & Schulten, K. Flexible fitting of atomic structures into electron microscopy maps using molecular dynamics. *Structure* **16**, 673–683 (2008).
49. Emsley, P., Lohkamp, B., Scott, W. G. & Cowtan, K. Features and development of Coot. *Acta Crystallogr. D Biol. Crystallogr.* **66**, 486–501 (2010).
50. Adams, P. D. et al. PHENIX: a comprehensive Python-based system for macromolecular structure solution. In *International Tables for Crystallography* 539–547 (2012).
51. Pettersen, E. F. et al. UCSF Chimera–a visualization system for exploratory research and analysis. *J. Comput. Chem.* **25**, 1605–1612 (2004).
52. Chen, V. B. et al. MolProbity: all-atom structure validation for macromolecular crystallography. *Acta Crystallogr. D Biol. Crystallogr.* **66**, 12–21 (2010).
53. Pintilie, G. et al. Measurement of atom resolvability in cryo-EM maps with Q-scores. *Nat. Methods* **17**, 328–334 (2020).
54. Pettersen, E. F. et al. UCSF ChimeraX: Structure visualization for researchers, educators, and developers. *Protein Sci.* **30**, 70–82 (2021).
55. Repen, B., Schneider, E. & Alexiev, U. Optimization of a malachite green assay for detection of ATP hydrolysis by solubilized membrane proteins. *Anal. Biochem.* **426**, 103–105 (2012).
56. Shindo, H., Furubayashi, A., Shimizu, M., Miyake, M. & Imamoto, F. Preferential binding of E.coli histone-like protein HU alpha to negatively supercoiled DNA. *Nucleic Acids Res.* **20**, 1553–1558 (1992).
57. Meades, G. Jr., Benson, B. K., Grove, A. & Waldrop, G. L. A tale of two functions: enzymatic activity and translational repression by carboxyltransferase. *Nucleic Acids Res.* **38**, 1217–1227 (2010).
58. Schneider, C. A., Rasband, W. S. & Eliceiri, K. W. NIH Image to ImageJ: 25 years of image analysis. *Nat. Methods* **9**, 671–675 (2012).

Acknowledgements

We thank the Cryo-EM Center at the University of Science and Technology of China (USTC) for their assistance with the experiments. This work was supported by the National Key R&D Program of China (2022YFA1302700 to K.Z. and 2022YFC2303700 to K.Z. and S.L.), the National Natural Science Foundation of China (32301044 to S.L. and 32371345 to K.Z.), Anhui Provincial Natural Science Foundation (2308085QC80 to S.L.), the Strategic Priority Research Program of the Chinese Academy of Sciences (XDB0490000 to K.Z.), the Center for Advanced Interdisciplinary Science and Biomedicine of IHM (QYPY20220019 to K.Z.), the Fundamental Research Funds for the Central Universities (WK9100000032 to S.L. and WK9100000044 to K.Z.), and the USTC start-up funding (KY9100000032, KY9100000056 and KJ2070000080 to K.Z.).

Author contributions

K.Z. and S.L. conceived the study and designed the experiments. X.Z. prepared the samples and performed cryo-EM sample preparation, screening, data collection, and image processing. Y. G. helped with data collection. K.Z. conducted final structure determination. S.L. built and refined the models. X.Z., Q.G., K.Z., and S.L. analyzed the data. K.Z. and S.L. wrote and edited the manuscript with input from all other authors.

Competing interests

The authors declare no competing interests.

Additional information

Supplementary information The online version contains supplementary material available at https://doi.org/10.1038/s41467-024-50722-1.

Correspondence and requests for materials should be addressed to Kaiming Zhang or Shanshan Li.

Peer review information *Nature Communications* thanks Yue Feng, Qun Liu, and the other anonymous, reviewer for their contribution to the peer review of this work. A peer review file is available.